



## **Influence of local geoid variation on water surface elevation estimates derived from multi-mission altimetry for Lake Namco**

**Jiang, Liguang; Andersen, Ole Baltazar; Nielsen, Karina; Zhang, Guoqing; Bauer-Gottwein, Peter**

*Published in:*  
Remote Sensing of Environment

*Link to article, DOI:*  
[10.1016/j.rse.2018.11.004](https://doi.org/10.1016/j.rse.2018.11.004)

*Publication date:*  
2019

*Document Version*  
Peer reviewed version

[Link back to DTU Orbit](#)

*Citation (APA):*  
Jiang, L., Andersen, O. B., Nielsen, K., Zhang, G., & Bauer-Gottwein, P. (2019). Influence of local geoid variation on water surface elevation estimates derived from multi-mission altimetry for Lake Namco. *Remote Sensing of Environment*, 221, 65-79. <https://doi.org/10.1016/j.rse.2018.11.004>

---

### **General rights**

Copyright and moral rights for the publications made accessible in the public portal are retained by the authors and/or other copyright owners and it is a condition of accessing publications that users recognise and abide by the legal requirements associated with these rights.

- Users may download and print one copy of any publication from the public portal for the purpose of private study or research.
- You may not further distribute the material or use it for any profit-making activity or commercial gain
- You may freely distribute the URL identifying the publication in the public portal

If you believe that this document breaches copyright please contact us providing details, and we will remove access to the work immediately and investigate your claim.

# **Influence of local geoid variation on water surface elevation estimates derived from multi-mission altimetry for Lake Namco**

**Liguang Jiang <sup>a,\*</sup>, Ole Baltazar Andersen <sup>b</sup>, Karina Nielsen <sup>b</sup>, Guoqing Zhang <sup>c, d</sup>, Peter Bauer-Gottwein <sup>a</sup>**

<sup>a</sup> Department of Environmental Engineering, Technical University of Denmark, 2800 Kgs. Lyngby, Denmark

<sup>b</sup> Division of Geodesy, National Space Institute, Technical University of Denmark, 2800 Kgs. Lyngby, Denmark

<sup>c</sup> Key Laboratory of Tibetan Environment Changes and Land Surface Processes, Institute of Tibetan Plateau Research, Chinese Academy of Sciences, Beijing 100101, China

<sup>d</sup> CAS Center for Excellence in Tibetan Plateau Earth Sciences, Beijing 100101, China

\* Corresponding author. Email address: [ljia@env.dtu.dk](mailto:ljia@env.dtu.dk)

1 **Abstract:** Water surface elevation (WSE) is an essential quantity for water resource  
2 monitoring and hydrodynamic modeling. Satellite altimetry has provided data for inland  
3 waters. The height that is derived from altimetry measurement is ellipsoidal height. In order  
4 to convert the ellipsoidal height to orthometric height, which has physical meaning, accurate  
5 estimates of the geoid are needed. This paper evaluates the suitability of geodetic altimetric  
6 measurements for improvement of global geoid models over a large lake in the Tibetan  
7 Plateau. CryoSat-2 and SARAL/AltiKa are used to derive the high-frequency geoid  
8 correction. A validation of the local geoid correction is performed with data from in-situ  
9 observations, a laser altimetry satellite (ICESat), a Ka-band radar altimetry satellite (SARAL)  
10 and a SAR radar altimetry satellite (Sentinel-3). Results indicate that, geodetic altimetric  
11 dataset can capture the high-resolution geoid information. By applying local geoid correction,  
12 the precision of ICESat, SARAL and Sentinel-3 retrievals are significantly improved. We  
13 conclude that using geodetic altimetry to correct for local geoid residual over large lakes  
14 significantly decreases the uncertainty of estimates of WSE. These results also indicate the  
15 potential of geodetic altimetry missions to determine local geoid residual with centimeter-  
16 level accuracy, which can be incorporated to improve global and regional geopotential models.

17 **Keywords:** satellite altimetry; CryoSat-2; water level; local geoid; Lake Namco

## 18 **1. Introduction**

19 Terrestrial freshwater is a crucial resource for all terrestrial life and human activities,  
20 although it represents less than 3% of the total water storage on the planet (Dingman, 2015).  
21 With increasing population, freshwater resources are under growing pressure in parts of the  
22 world, and managers face difficult trade-offs between human needs for water and ecosystem  
23 water requirements. Water surface elevation (WSE) is one of the most important quantities for  
24 hydrological research, as it is closely related to water storage and exchange fluxes in lakes,  
25 wetlands, reservoirs, and rivers. WSE change and variability (i.e. annual, interannual, and  
26 intraseasonal variability) are important indicators for climate change. However, limited

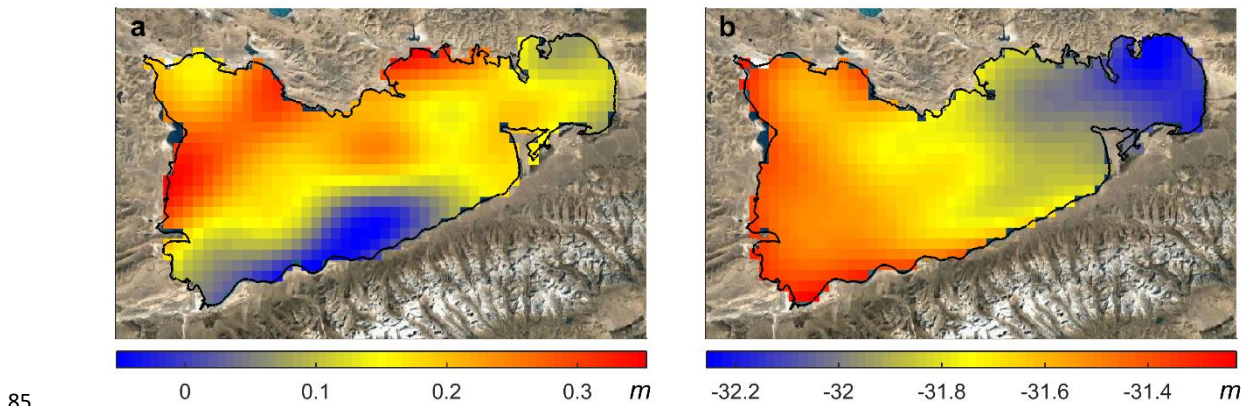
27 availability of in-situ monitoring data impedes comprehensive research of inland hydrology and  
28 water resources management (e.g. the spatial and temporal dynamics of freshwater storage,  
29 flood forecasting, etc.) especially in developing countries (Alsdorf et al., 2007). Technological  
30 advances in recent satellite altimeter missions (e.g. Jason-2/-3, CryoSat-2, SARAL/AltiKa,  
31 Sentinel-3, etc.), provide alternative options of measuring WSE of inland water bodies. WSE  
32 derived from satellite altimetry is becoming increasingly used for inland water monitoring and  
33 hydrodynamic modeling in the hydrology community (e.g. Crétaux et al., 2011; Jiang et al.,  
34 2017a, 2017b, Schneider et al., 2018a, 2018b, 2017; Schwatke et al., 2015 among others).  
35 Compared to short-repeat missions, e.g. Envisat and Jason, geodetic missions, for example,  
36 CryoSat-2, have distinct advantages for surface water monitoring because of the drifting ground  
37 track pattern. With its roughly 8 km ground track spacing at the equator, it detects much more  
38 water bodies than any other satellite (Jiang et al., 2017c). However, CryoSat-2's 369 days repeat  
39 prevents it from capturing the seasonal signal in small lakes (Nielsen et al., 2015).

40 The principal of satellite radar altimetry is to measure the travel time of a microwave pulse  
41 traveling between the altimeter and water surface, which can be converted into a distance (i.e.  
42 range  $R$ ). The ellipsoidal height is obtained from orbit height above a reference ellipsoid ( $h$ ) by  
43 subtracting the measured range  $R$ . The altimeter observes within a range window, which is  
44 typically between 30 m and 120 m depending on the instrument. The closed-loop tracking  
45 (autonomous tracking) system will fail to track the correct range if there are abrupt elevation  
46 changes in the terrain exceeding this range (Biancamaria et al., 2017; Dehecq et al., 2013). This  
47 is because the closed-loop tracker is heavily dependent on previous measurements for current  
48 estimates of range and range rate (Chelton et al., 2001). That is to say, water bodies surrounded  
49 by or adjacent to steep mountains are prone to be incorrectly measured. Additionally, due to  
50 the large footprint, the inhomogeneous ground surface can lead to incorrect measurements.  
51 Therefore, inland water altimetry data can suffer from degradation in quality due to the  
52 contamination of surroundings and inaccurate corrections (Abulaitjiang et al., 2015).

53           However, the location of a reference ellipsoid is arbitrary in the sense that its center does  
54 not coincide with the mass center of the Earth, so ellipsoidal heights have no relationship to  
55 gravity and do not give an accurate portrayal of how water flows (Meyer et al., 2006). Instead,  
56 the dynamic height is an equipotential surface and water will not flow of the same height  
57 (Heiskanen and Moritz, 1967). Nevertheless, dynamic heights are not suitable as practical  
58 heights because they are not geometric distances and a large correction that accounts for gravity  
59 is needed. See detailed explanation in Heiskanen and Moritz (1967) and Meyer et al. (2006).  
60 Orthometric height is widely used in engineering and environmental activities due to its  
61 physical and geometric meaning and ability to predict fluid flows in many situations (Erol,  
62 2011; Heiskanen and Moritz, 1967; Yilmaz, 2008). Orthometric height is approximated by  
63 subtracting geoid height from ellipsoid height. Therefore, an accurate geoid model is needed to  
64 convert ellipsoidal heights to orthometric heights.

65           The idealized of equipotential surface of the oceans was proposed as the “mathematical  
66 figure of the Earth” and was later termed the “geoid” (Heiskanen and Moritz, 1967). There have  
67 been many definitions of the “geoid” and NGS defines it as “*the equipotential surface of the*  
68 *Earth's gravity field which best fits, in the least squares sense, global mean sea level*” (National  
69 Geodetic Survey, 1986). The geoid height ( $N$ ), also called geoid undulation, is defined as “*the*  
70 *distance, taken along a perpendicular to the ellipsoid of reference, from that ellipsoid to the*  
71 *geoid*” (National Geodetic Survey, 1986). This height varies with location from -107 to 86 m,  
72 and the uncertainties of the current most accurate global geoid models (GGMs) are about 18.3  
73 cm for the land areas according to the EGM2008 (Pavlis et al., 2012). Global geoid models  
74 such as EGM2008, do not represent high frequency geoid undulations (i.e. within 5 arc mins or  
75 ~9 km). This problem is known as the omission error in gravity field modeling (Hirt et al.,  
76 2010). However, the Earth’s geoid has significant structure at smaller scales (Mazloff et al.,  
77 2014). Several studies have indicated that this problem is more severe over rugged mountainous  
78 areas, like the Himalaya and the Andes due to the too sparse terrestrial gravity data used in  
79 GGMs (Li et al., 2015; Pavlis et al., 2012; She et al., 2016). Fig. 1 shows the height difference

80 between two widely used geoid models over the Lake Namco on Tibetan Plateau. The  
81 difference is in the range of - 0.05 to 0.35 m with significant structure, which can result in errors  
82 if e.g., altimetry is averaged along track to derive mean height of the lake. Therefore, an  
83 imprecise geoid model can affect the estimated WSE (especially for long-repeat missions) and  
84 hydrodynamic simulations.



86 **Fig. 1.** Illustration of (a) geoid height difference between EGM2008 (Pavlis et al., 2012) and  
87 GOCO05c (Fecher et al., 2017) and (b) EGM2008 height over the Lake Namco in Tibetan  
88 Plateau

89 Over the past decade, many studies have investigated changes in WSE of lakes over the  
90 Himalaya regions (Hwang et al., 2016; Jiang et al., 2017a; Song et al., 2014; Tseng et al., 2016;  
91 Zhang et al., 2011) with the increasing availability of altimetry data sets. However, time series  
92 for lakes in these mountainous regions need to be carefully processed. The reason is twofold as  
93 aforementioned: first, inaccurate measurements may be included if the complete open water  
94 mask is used to select the altimetry data; second, local geoid variations can induce large  
95 uncertainty because those variations can reach amplitudes of 15 cm or even larger in  
96 mountainous areas for GGMs (Hirt, 2011). This error would probably be propagated into model  
97 simulation when hydrodynamic numerical models are used for nutrient management,  
98 biogeochemical processes simulation, hydraulic structures, etc. (Seo et al., 2010; Xue et al.,  
99 2017; Zandagba et al., 2016). This issue is especially important for geodetic missions, like  
100 CryoSat-2 and SARAL, due to geoid height variation along and across ground tracks.

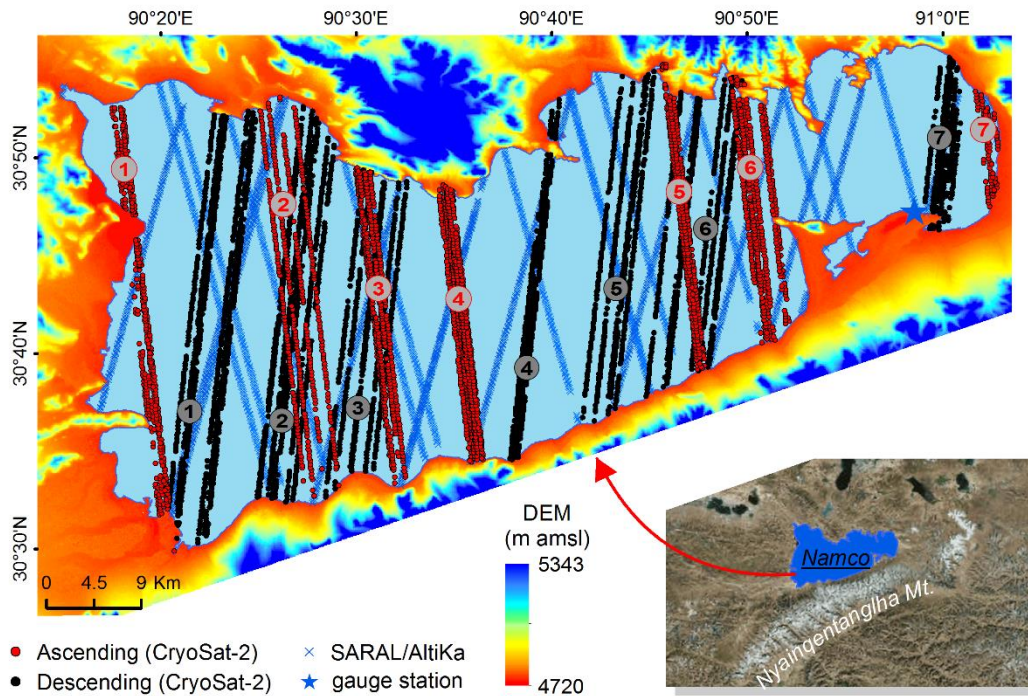
101 Kleinherenbrink et al. (2014) briefly mentioned that the inaccuracy in geoid model can induce  
102 water surface slope. Crétaux et al. (Crétaux et al., 2011) also emphasized that it is necessary to  
103 correct for the slope of the geoid because geoid models do not correctly map high-frequency  
104 variations over large lakes.

105 The aim of this paper is to exploit satellite radar altimetry data in improving local geoid  
106 estimates over inland waters. To this end, we collect altimetry data from different missions, i.e.,  
107 CryoSat-2, SARAL, Sentinel-3 and ICESat. Here, we derive a local geoid correction field using  
108 geodetic measurements from CryoSat-2 and SARAL (drifting phase). Furthermore, we use  
109 high-resolution ICESat data to validate the improved geoid model (EGM2008). Finally, we  
110 extend the validation to SARAL and Sentinel-3 to demonstrate the effect of geoid variations on  
111 WSE estimates.

## 112 **2. Materials and Methods**

### 113 *2.1. Study site*

114 Lake Namco is the second largest lake on the Tibetan Plateau with an area of about 2024  
115 km<sup>2</sup> and a maximum depth of over 90 m (Wang et al., 2009). It is an endorheic lake bounded  
116 by the Nyainqentanglha Mountains in the south, and several small mountains in the north (Fig.  
117 2). It is replenished by precipitation and glacier melting runoff. The tributaries are mainly  
118 coming from the west and the south. Namco is located on the northeast flank of  
119 Nyainqentanglha Mountains. The lake generally stretches from west to east with a length of  
120 over 70 km and is well sampled by CryoSat-2. The lake level has risen rapidly over the last two  
121 decades (Lei et al., 2013), and it is still rising (Jiang et al., 2017a). This lake is chosen for two  
122 reasons; it is large enough, which allows us to solve short-wavelength variation and it is close  
123 to high mountains where the geoid models are affected by topographic effect (Akyilmaz et al.,  
124 2009; Forsberg, 1985).



125

126

**Fig. 2.** Map of the study area. The background is ALOS digital surface model with CryoSat-2 and SARAL/AltiKa altimetric measurements overlaid. Numbers indicate the groups containing several ascending/descending ground tracks of CryoSat-2.

127

128

129 *2.1. CryoSat-2 20 Hz SARIn waveforms and data handling*

130

131

132

133

134

135

136

137

CryoSat-2 is the first altimetry mission carrying a spaceborne Synthetic Aperture Interferometric Radar Altimeter (SIRAL), which is a state-of-the-art altimeter working in three modes, i.e. low resolution mode (LRM), synthetic aperture mode (SAR), and synthetic aperture interferometric mode (SARIn). SAR mode provides data with a finer along-track spatial resolution (ca. 300m). In SARIn mode two antennas are combined to determine the cross-track angle of arrival of the radar echoes. SARIn mode is activated over the ice-sheet margins, mountain areas, and some other regions, such as Danube River, Congo River, etc. (European Space Agency and Mullar Space Science Laboratory, 2012; Jiang et al., 2017c).

138

139

140

The data used in this study is the baseline C level 1b (L1b) dataset provided by ESA. L1b data files contain geolocated and time stamped waveforms with accompanying altitude, position, corrections, interferometric phase difference, coherence waveforms, etc. Please refer

141 to CryoSat-2 Product Handbook (European Space Agency and Mullar Space Science  
142 Laboratory, 2012) for a detailed description.

143 The CryoSat-2 L1b data were retracked with a narrow primary peak threshold (NPPT)  
144 retracker (Jain et al., 2015). The chosen threshold depends on the underlying surface, with lower  
145 thresholds for ocean and ice sheets, and higher thresholds for inland waters. In this study, we  
146 used 80% to determine the retracking point (Villadsen et al., 2016). We alternatively examined  
147 the default ESA retracker and a Gaussian threshold retracker, but NPPT with a threshold of  
148 80% was most stable. Moreover, SARIn mode data allows us to locate the cross-track location  
149 of scatterers (Abulaitijiang et al., 2015). In this study, we only used measurements from nadir.

150

## 151 2.2. SARAL/AltiKa data

152 SARAL/AltiKa is the first altimeter measuring in Ka-band frequency. Measurements in  
153 the Ka-band have a reduced footprint (4-5 km in radius) which results in higher spatial  
154 resolution. Another improvement of AltiKa is its enhanced bandwidth (500 MHz), which leads  
155 to higher vertical resolution and higher pulse repetition frequency (CNES, 2016). Therefore, it  
156 is expected to increase precision and data availability (along-track sampling at 40 Hz) and  
157 thereby increase sensitivity to the geoid anomaly over inland water located in sloping terrain  
158 (Steunou et al., 2015). The SARAL satellite flew on the same repeat orbit as ENVISAT with a  
159 35-day repeat cycle until July 2016, and was then switched to drifting orbit mode.

160 Geophysical Data Records (GDRs) during 2013 and 2016 were downloaded from CNES  
161 AVISO+ program (Centre National D'Etudes Spatiales, Archiving, Validation and  
162 Interpretation of Satellite Oceanographic data, <ftp://avisoftp.cnes.fr/AVISO/pub/>). During the  
163 repetitive orbit phase, there are two orbits passing across Lake Namco, i.e. ascending track  
164 number 165 and descending track number 524. For some cycles, the ground track deviates ~10  
165 km (depending on the altitude) away from its nominal position. In addition, some cycles have  
166 fewer measurements, which do not cover a long distance. In this study, these cycles were not

167 used. Moreover, we also use data measured during the drifting phase, i.e. cycle number from  
168 100, for retrieval of local geoid undulation.

### 169 *2.3. ICESat/GLAS data*

170 The Geoscience Laser Altimeter System (GLAS) on ICESat satellite uses a laser system  
171 to measure the range, which uses short pulses (6 ns) of infrared light (1064 nm) and visible  
172 light (532 nm). The resolution is ~70 m (footprint diameter) and the spatial sampling along-  
173 track is 170 m. The precision of ICESat measurements of flat surfaces is 2 cm within footprint  
174 size (Zwally et al., 2008). This can help to measure WSE close to the lakeshore and to detect  
175 the supposed local geoid residual. ICESat operated during 2003 to 2010. Unfortunately, ICESat  
176 suffered from a problem with the onboard lasers, which means that it could only produce data  
177 2-3 times per year. In total, 43 overflights of ICESat/GLA14 altimetry data are available over  
178 Lake Namco.

### 179 *2.4. Sentinel-3/SRAL data*

180 A dual-frequency SAR radar altimeter (SRAL) on Sentinel-3 satellite, has some new  
181 features. It covers the Earth entirely in the SAR mode, which is designed to achieve finer along-  
182 track resolution. This property facilitates water surface height measurement close to the coastal  
183 areas. Another important characteristic is the tracking mode, i.e. open-loop tracking mode  
184 where the altimeter range window is well positioned based on a priori on-board DEM.  
185 Therefore, tracking over surfaces with sudden elevation changes is more robust. A detailed  
186 introduction can be found in Sentinel-3 User Handbook.

### 187 *2.5. WSE from altimetry*

188 Ranges of all altimetric datasets were first corrected using the associated parameters, i.e.  
189 ionosphere correction, dry and wet troposphere corrections, polar tide correction, solid earth  
190 tide, retracker correction, geoid height (Jain et al., 2015; Nielsen et al., 2015). Then WSE was  
191 calculated using following equation:

192 
$$R_c = R - R_{rrk} - R_{geo} \quad (1)$$

193 
$$WSE = h - R_c - N \quad (2)$$

194 Here,  $h$  is satellite altitude above the reference ellipsoid,  $R$  is onboard tracker range,  $R_{rrk}$  is  
195 retracking correction,  $R_{geo}$  is the sum of geophysical corrections, and  $N$  is geoid height  
196 referenced to EGM2008.

197 *2.6. Outlier removal*

198 To filter outliers in each track, we excluded those beyond two deviations on either side of  
199 the median value. As the measurement distribution contain outliers, standard deviation would  
200 not yield a representative value. Therefore, a well-known robust estimator of deviation was  
201 used, i.e., the median of absolute deviation (MAD). Different from the method of mean plus or  
202 minus three standard deviations, which is based on a Gaussian distribution, the MAD is more  
203 robust in case of the distribution of water levels is non-Gaussian (Blewitt et al., 2016; Leys et  
204 al., 2013). Following steps explain the estimate of deviation.

205 Step 1: calculate the median of all measurements:  $M = \text{median}(WSE)$

206 Step 2: calculate the absolute deviations from median:  $AD = \text{abs}(WSE - M)$

207 Step 3: calculate the median of absolute deviations:  $MAD = \text{median}(AD)$

208 Step 4: calculate the deviation:  $\sigma = 1.4826 \text{ MAD}$

209 Therefore, measurements within the range of  $[M - 2\sigma, M + 2\sigma]$  were used. This procedure  
210 was applied to all altimetry data sets.

211 *2.7. Local geoid correction computing*

212 Given that the lake surface in hydrostatic equilibrium theoretically represents a gravity  
213 potential isosurface (Zlinszky et al., 2014), i.e. dynamic height of the lake is equal everywhere  
214 over the lake (Heiskanen and Moritz, 1967), we assume that this equipotential surface mimics  
215 the geoid. Considering that the variation of acceleration of gravity is much smaller than geoid  
216 uncertainty at the spatial scale we are investigating, we assume the difference of along-track  
217 anomalies between dynamic height and orthometric height is negligible (Heiskanen and Moritz,

218 1967). Put it differently, we assume that the orthometric height of the lake surface as nearly  
219 constant. WSE anomaly of each track was obtained by subtracting the along-track mean value.  
220 Therefore the WSE anomaly is mainly subject to geoid residual (Pavlis et al., 2012), which is  
221 the short-wavelength variation not solved in global geoid models. By applying Eq. (3) for  
222 individual track, anomaly, i.e.  $H_a$  over the lake is obtained. Further, a local geoid correction  
223 filed can be determined by interpolation, and then spatially filtering of  $H_a$ .

$$224 \quad H_a = WSE - \text{mean}(WSE) \quad (3)$$

225

### 226 **3. Results**

#### 227 *3.1. Estimated water levels*

228 As we can see from Fig. 3, the measurements close to the lakeshore are severely corrupted  
229 when CryoSat-2 flies from south to north (ascending orbit). In most cases, the first 15 - 20  
230 measurements are overestimated, which leads to an upward slope instead of a horizontal line in  
231 the height profile. Taking group 5 (see Fig. 2) as an example, in this case, even 6 km away from  
232 lakeshore, the WSE is still overestimated (Fig. 3). However, when the ground track is  
233 approaching to the lakeshore (from water to land), the observation is barely affected although  
234 the mountain is very close (Figs. 2 and 3). Similarly, when CryoSat-2 flies in descending orbit  
235 (from north to south), the northern part of the lake is overestimated while the south part is  
236 correctly measured (Fig. 4). It should be noted that this effect only occurs when the ground  
237 track goes from land to water and the elevation change is steep (larger than the tracking  
238 window). This is different from the effect of land contamination, which occurs when the  
239 footprint partially illuminates land areas and does not depend on the flight direction. We will  
240 address the nature of these noisy water levels in the discussion.

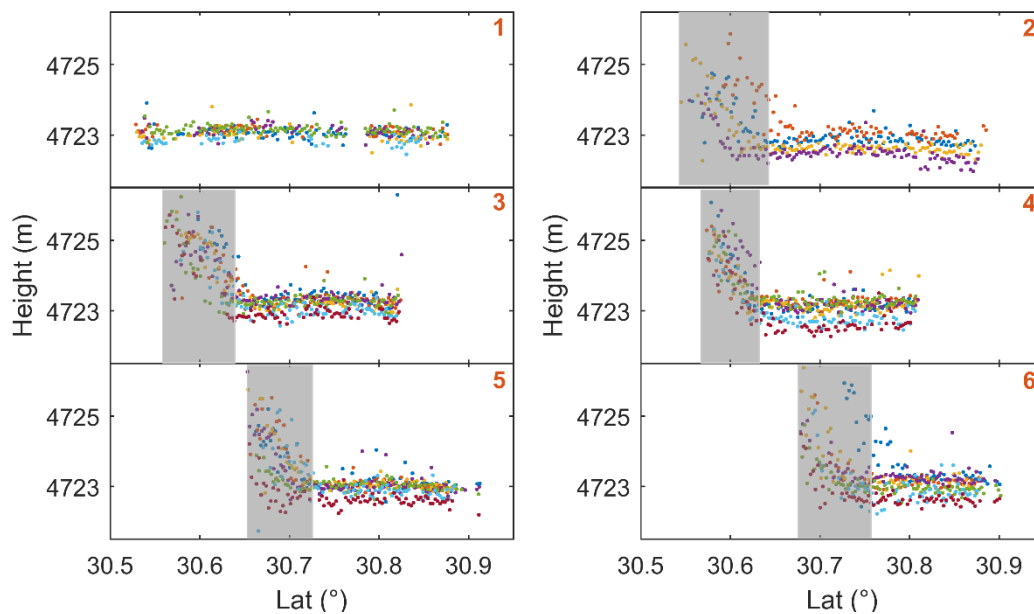
241 Because the weaker geoid residual may be hidden in the noisy water levels, they are  
242 excluded in the further analysis. More specifically, for CryoSat-2 ascending tracks, the  
243 measurements within 6 km from southern lakeshore were discarded. Similarly, for descending

244 tracks, those within 6 km from northern lakeshore were excluded. Thus, the remaining  
245 measurements still cover the lakeshore areas. Six km is based on visual examination. Moreover,  
246 we also excluded the measurements during ice-bound period, i.e. 1<sup>st</sup> January to 31<sup>st</sup> May (Ke et  
247 al., 2013; Kropáček et al., 2013).

248 In order to better sample the whole lake, we also used data from SARAL during the drifting  
249 phase (hereafter as SARAL-DF). SARAL-DF also have noisy water level elevations over the  
250 lakeshore areas, therefore we excluded those within 2 km from shoreline. Similarly,  
251 measurements during cold season were removed. See the distribution of measurements in Fig.  
252 1.

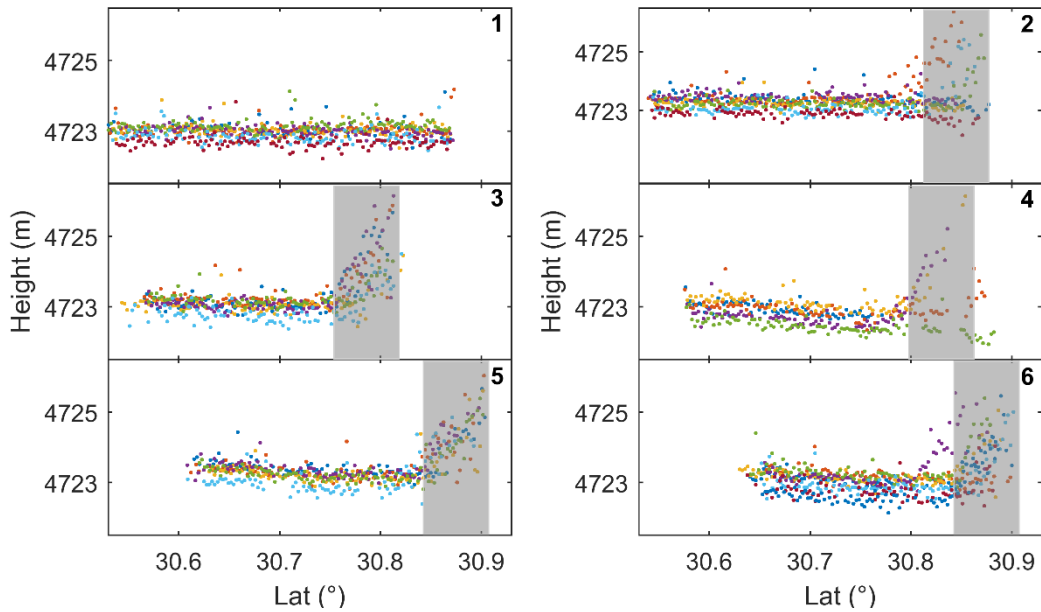
253

254



255

256 **Fig. 3.** Along-track measurement profiles of ascending tracks from Cryosat-2, i.e. satellite  
257 flies from low latitude to high latitude. Color corresponds to individual track. Number of each  
258 plot please refer to group number in Fig. 2. Grey box highlights the incorrect measurements.

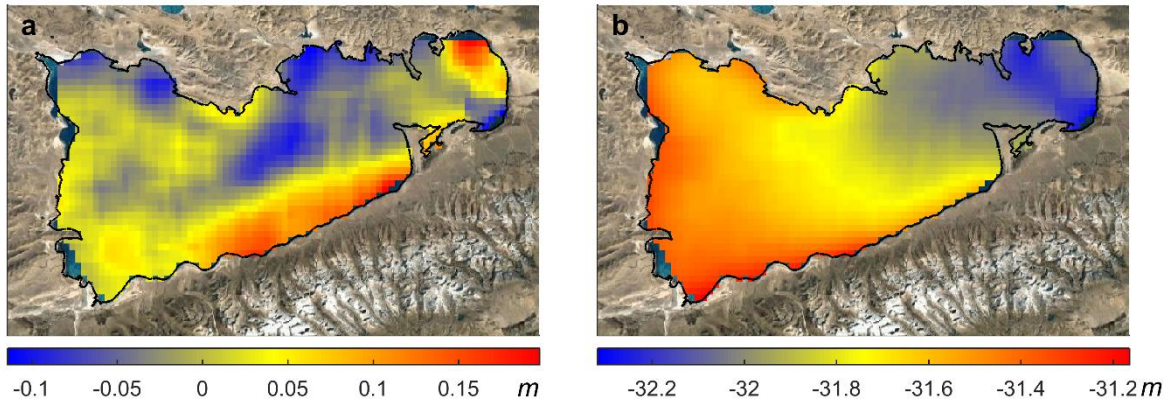


259

260 **Fig. 4.** Along-track measurement profiles of descending tracks from Cryosat-2, i.e. satellite  
 261 flies from high latitude to low latitude. Color corresponds to individual track. Number of each  
 262 plot please refer to group number in Fig. 2. Grey box highlights the incorrect measurements.

263 *3.2. Small-scale geoid signal and geoid variation*

264 Fig. 5 displays local geoid correction field and corresponding corrected EGM2008 geoid  
 265 model over Lake Namco. The correction is of a few decimeters and shows significant small-  
 266 scale structure. Large corrections are along the south lakeshore, where it is in the magnitude of  
 267 15 cm. As expected, the geoid is underestimated (positive correction) close to the  
 268 Nyainqentanglha Mountains (i.e. the red-coded pixels in Fig. 5a) because the mountain mass  
 269 outside the geoid is not correctly solved in spherical harmonic models. Therefore, it can be  
 270 argued that the impact of the high-frequency terrain effect on geoid is noticeable. It is likely  
 271 that correction in the northeast corner is a bit overestimated due to less altimetric measurements  
 272 are used. Nevertheless, the magnitude of local geoid correction is close to the claim that the  
 273 RMS of EGM2008 commission error for land is  $\pm 18.3$  cm (Pavlis et al., 2012). We created a  
 274 finer geoid model by adding this local geoid correction to EGM2008 (Fig. 5b). It is obvious  
 275 that the new geoid mode exhibits a gentle southwestward slope (1/70 000).



276

277

278

279

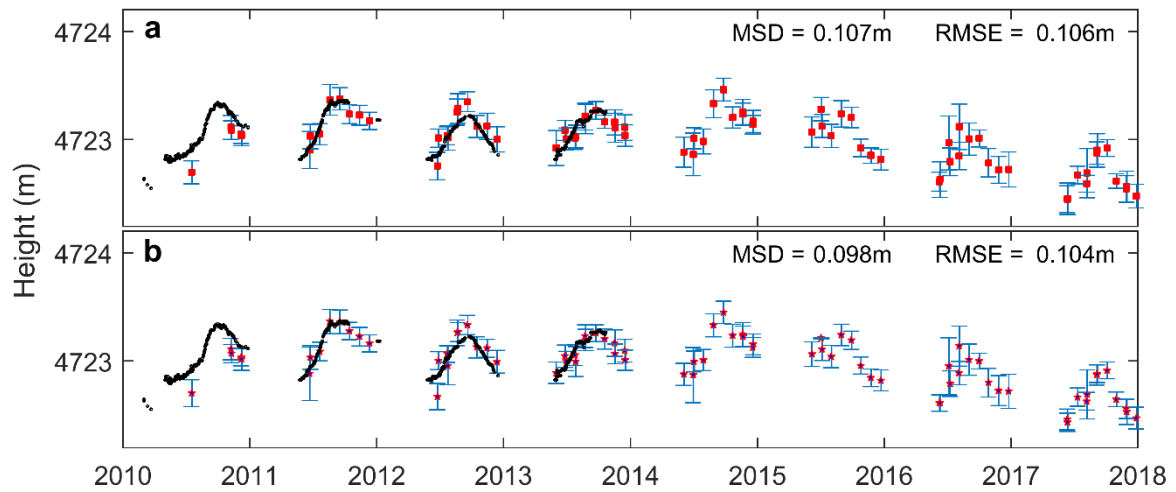
**Fig. 5.** (a) Map of interpolated local geoid correction derived from CryoSat-2 and SARAL-DF. Cubic interpolation was used to create this map. (b) Map of corrected EGM2008 geoid model with local geoid correction added.

280

281

282

As shown in Fig. 6, WSE derived from CryoSat-2 generally agrees well with gauge data. On the other hand, accounting for local geoid residual indeed helps to improve WSE precision and accuracy by 8% and 2%, respectively.



283

284

285

286

**Fig. 6.** Time series of WSE derived from CryoSat-2 against in-situ measurements. Black square is in-situ measurement with vertical bias added. Bar indicates standard deviation. (a) WSE is referenced to EGM2008 and (b) WSE is referenced to corrected EGM2008.

287

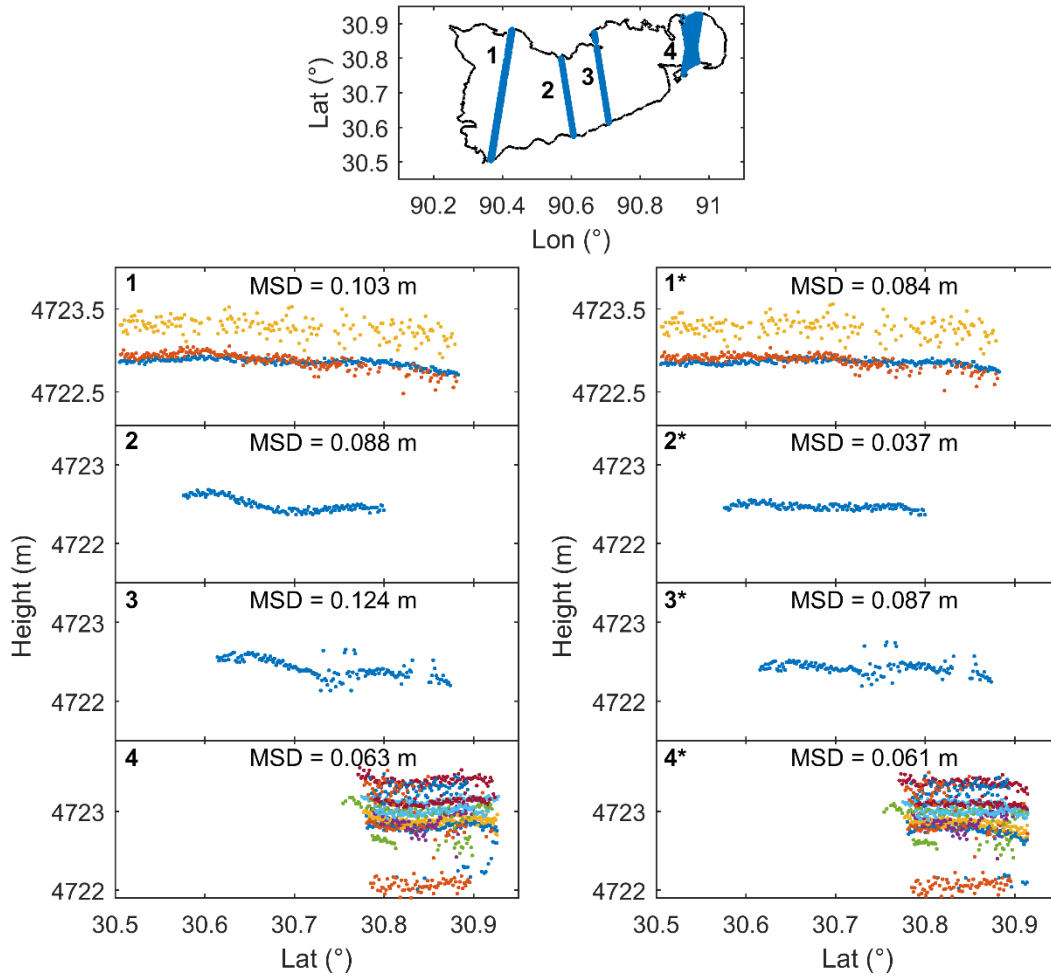
### 3.3. Validation

288 In this section, we validate the local geoid correction field by comparing the standard  
289 deviation of measurements per track before and after applying this correction. Median of the  
290 standard deviation (MSD) is used to evaluate the performance for three data sets. As stated in  
291 Section 2, we only use measurements during ice-free period.

### 292 3.3.1. ICESat

293 There are 21 out of 43 tracks crossing Lake Namco. As shown in Fig. 7, these tracks mainly  
294 transect four locations and thus we categorized them into 4 groups. Groups 1-3 show clear  
295 curving shapes in the height profiles. The geoid close to the south lakeshore is underestimated  
296 due to the mountain ranges (see Fig. 2). After applying the local geoid correction, ICESat height  
297 profiles are almost horizontal, especially for the first 3 groups which have long cross-over  
298 distance ( $> 20$  km).

299 Data precision before and after applying the local geoid correction was evaluated in terms  
300 of MSD. MSDs of most tracks (14/21) are reduced and the MSD of all tracks decreases from  
301 0.070 m to 0.064 m. For the second and third groups, the improvement of precision is striking,  
302 i.e. by 58% and 30% on average, respectively. For group 3 (only one track), the correction has  
303 a positive effect although the statistics is not very high due to several peaky measurements (Fig.  
304 7). In contrast, group 4 does not improve much. This is probably because the small-scale geoid  
305 variations in the eastern part of Namco is less significant (Fig. 5).



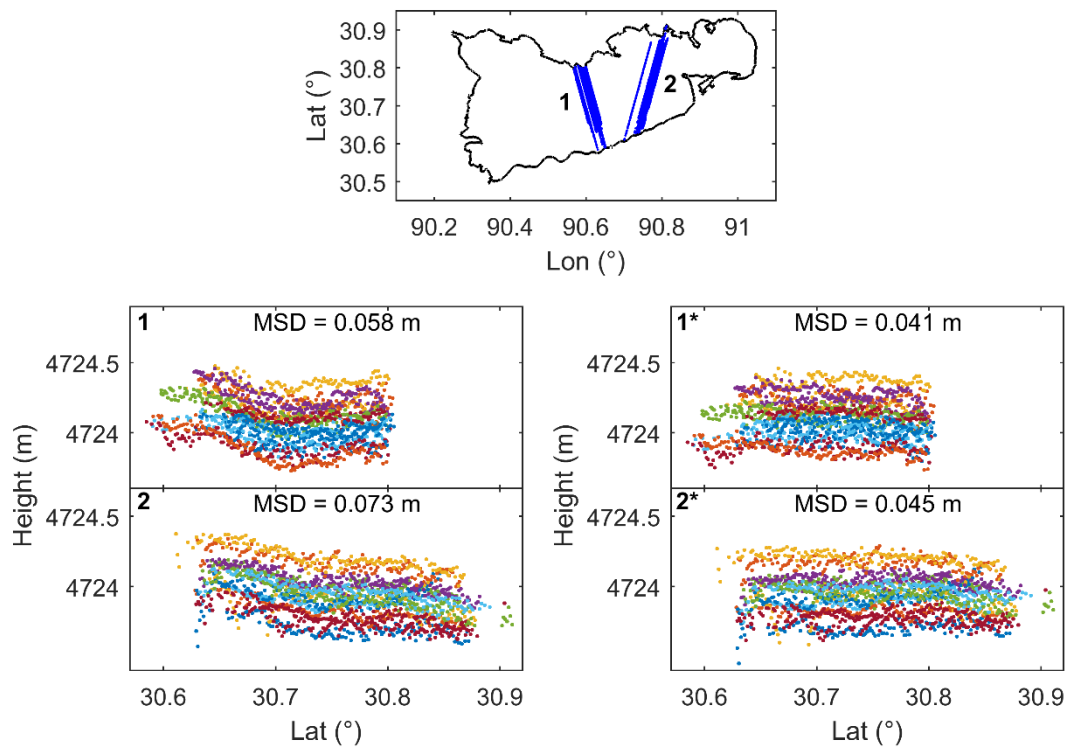
306

307 **Fig. 7.** Along-track measurement profiles from ICESat. Numbers in the bottom four rows are  
 308 shown in top figure (\* indicates corrected one). The data are referenced to EGM2008 (left  
 309 column) and our enhanced EGM2008 (right column). By referencing to the improved geoid,  
 310 the profiles become better levelled. See the median standard deviation (MSD) in each plot.

### 311 3.3.2. SARAL

312 Similar to ICESat, SARAL also presents curving shapes in water height profiles (Fig. 8).  
 313 Group 1 shows the same curve shape as group 2 of ICESat, i.e., the WSE increases from the  
 314 lowest point at around  $30.71^\circ$  to both sides. Again, curving is effectively removed by correction  
 315 for local geoid residuals. Here group 2 exhibits a significant slope, which obviously cannot be  
 316 left out. Similarly, height profiles are almost level when considering local geoid correction. As  
 317 shown in Fig. 8, MSD is significantly improved. It is worthwhile to mention that the MSD of  
 318 all measurements is decreasing from 7 cm to 4.4 cm, which is slightly better than that of ICESat.

319 Note that, for most cycles, missing measurements are mainly the first few kms to the  
 320 lakeshore, especially for group 1 (Fig. 8). This is also seen in other cycles in drifting phase  
 321 (Fig. 2). This is mainly related to altimeter tracking performance over sloping terrain, especially  
 322 over regions with high relief as stated in Quality Assessment Report  
 323 (<ftp://avisoftp.cnes.fr/AVISO/pub/saral/>).



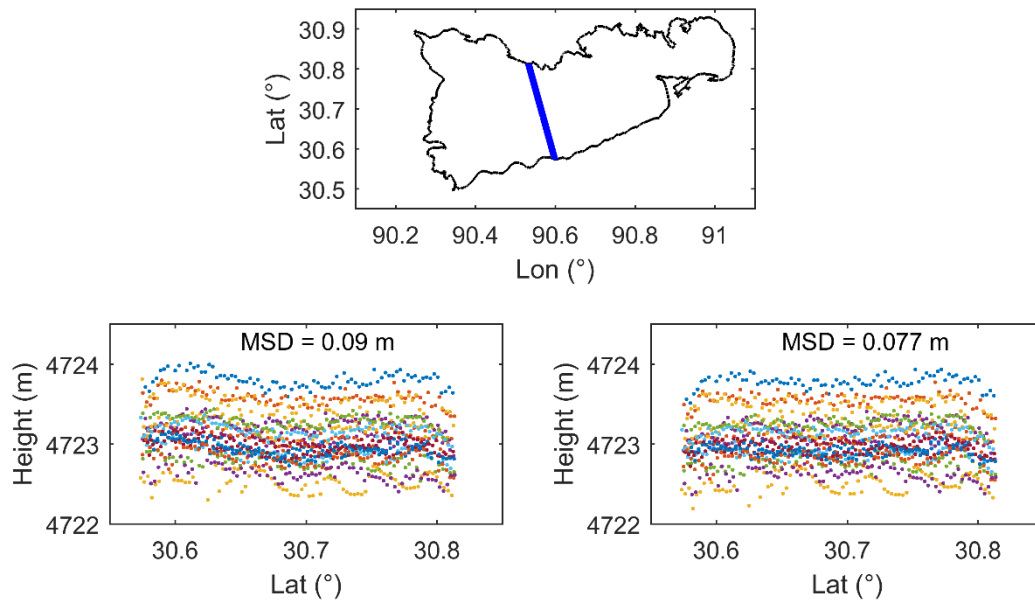
324

325 **Fig. 8.** Along-track measurement profiles of repeat tracks from SARAL. Numbers in the  
 326 bottom four rows are shown in top figure (\* indicates corrected one). Data are referenced to  
 327 EGM2008 (left column) and enhanced EGM2008 (right column). Median standard deviation  
 328 (MSD) is given in each plot.

### 329 3.3.3. Sentinel-3

330 As shown in Fig. 9, a trough appears in the middle of the tracks, i.e. around 30.7 °N,  
 331 showing a very similar pattern as exhibited in group 1 of SARAL. As we can see, it is improved  
 332 in visual and statistical manners after geoid correction applied (9 cm vs 7.7 cm). Compared  
 333 with ICESat and SARAL, MSD of Sentinel-3 is slightly larger. However, we can also see that

334 Sentinel-3 does not have noisy water levels, and measurements are much better than those of  
335 CryoSat-2 and SARAL in coast regions (Fig. 9).



336

337 **Fig. 9.** Along-track measurement profiles of tracks from Sentinel-3. Data are referenced to  
338 EGM2008 (left column) and enhanced EGM2008 (right column). Median standard deviation  
339 (MSD) is given in each plot.

#### 340 4. Discussion

341 The reflected signal suffers from land contamination near the water-land transition zone.  
342 In general, the degree of contamination is related to orientation and size of the altimeter  
343 footprint. In this sense, the signal from SARAL is prone to be contaminated by bright off-nadir  
344 features due to its large footprint (8 km in diameter). While, for CryoSat-2, it is less likely that  
345 the signal is affected at a few kms from lakeshore due to its smaller footprint (~ 300 m or 380  
346 m if the Hamming window is applied, along-track and 15 km across-track). Previous studies  
347 also demonstrated the high performance of SAR/SARIn altimetry over inland water (Nielsen  
348 et al., 2017; Villadsen et al., 2016). However, in this study, the nearshore lake level estimates  
349 are too high and the precision (i.e. MSD) is worse than that of SARAL although the latter has  
350 a footprint of 8 km (in diameter).

351 As shown in previous sections, Sentinel-3 has the same footprint as CryoSat-2, but it is  
352 not influenced by topography. To understand this difference between the water levels obtained  
353 from CryoSat-2 and Sentinel-3 we investigated both the multi-looked waveform and the stack  
354 (the individual waveforms from all looks) from both missions. We find that the performance of  
355 CryoSat-2 is closely related to topography. The CryoSat-2 waveforms are noisy when the  
356 satellite is flying over mountains towards the lake (see Figs A1 and A2 in Appendix A).  
357 However, the waveforms close to lakeshore are still good when the satellite is approaching the  
358 mountains (see Fig. A3 in Appendix A). This is not observed in the Sentinel-3 waveforms (see  
359 Figs. B1-B3 in Appendix B). The reason for the noisy CryoSat-2 waveforms is found in the  
360 stack (see Fig. C2 in Appendix C). In the nearshore measurements only a few looks capture the  
361 water surface. This is most likely because the tracking window is still adjusted to the higher  
362 topography for most of the bursts that is used to form the multi-looked waveform. When only  
363 a few looks are available the multi-looked waveform will as a consequence be noisier. As the  
364 satellite gets further away from the shore, more looks capture the water surface resulting in a  
365 gradually smoother waveform (see Figs A1, A2, and C2 in Appendix A and C). On the contrary,  
366 when satellite moves away from the lake, even a few kms away from lake, the backward-  
367 looking looks can still detect water, because the tracking window is still positioned referencing  
368 to the lake elevation instead of the higher mountain elevation. Moreover, As shown in Appendix  
369 C, CryoSat-2 multi-looks from different bursts are probably misaligned in range, which leads  
370 to unwanted smearing of multi-looked waveform after the multi-looking processing (Dinardo  
371 and Benveniste, 2013). This is different from Sentinel-3 looks, where a part of the looks are  
372 removed leading to a ‘clean’ multi-looked stack (Appendix C). Hence, we anticipate that the  
373 noisy water levels shown in Figs. 3 and 4 are due to errors in the retracking because of the noisy  
374 waveforms. It is unlikely that waveforms are polluted by land because the measurements at the  
375 moment the satellite moves away from the lake have the same condition (i.e. footprint covers  
376 both water and land) as those measured when the satellite moves towards the lake from land.  
377 This can also be justified by CryoSat-2 and Sentinel-3 waveforms (see waveforms in Appendix

378 A and B). Therefore, this problem is very likely attributed to CryoSat-2 processor and a slowly  
379 adjusting tracker. It is beyond the focus of this study. However, even though we do not know  
380 the exact problem with CryoSat-2 altimeter instrument, it does have problems over rugged high  
381 relief mountainous regions. In this regard, Sentinel-3 data outperforms the CryoSat-2 data.

382 Laser altimetry (e.g. ICESat) seamlessly measures across land-water transitions due to the  
383 smaller laser footprint (Zwally et al., 2002). Radar altimeters, which operate in low resolution  
384 mode, suffers from the off-nadir ranging due to large footprint, and limitations in the ability to  
385 determine a precise geolocated elevation (Brenner et al., 2007). The error contributions  
386 ('budget') to water WSE measurements derived from satellite altimetry, mainly arise from the  
387 instrument system, such as orbit determination error, range error, angle determination error,  
388 etc., and other atmospheric and geophysical corrections (Wingham et al., 2006; Zwally et al.,  
389 2002). Considering that the range error dominates the root-sum-square (RSS) of the error  
390 budget (on the order of 10 cm), smaller footprint and high pulse repetition frequency could be  
391 helpful to mitigate the range error, which has already shown by Sentinel-3 and SARAL  
392 (Bonfond et al., 2018).

393 On the other hand, geoid model error (on the order of  $\pm 18$  cm of EGM2008) will affect  
394 orthometric height, which is most commonly used in hydrology. The influence of geoid  
395 variations on inland water height estimates is not well studied and understood. It should be kept  
396 in mind that this can be important source of error in WSE time series construction from drifting  
397 ground-track datasets and hydrodynamic modelling, especially in mountainous areas because  
398 current global geoid models have larger uncertainty at local scale. In our study, the results show  
399 that local geoid variations omitted in global geoid models contributes significantly to the  
400 uncertainty of altimetry-based estimates of WSE. This will have an impact on monitoring of  
401 lake surface changes, especially for those having changes in the order of magnitude of a few  
402 centimeters. Even in the lowland area, the local geoid height induces uncertainty to WSE.

403 Naturally, we can derive the mean lake level for a track even if the surface is sloping  
404 (inaccurate geoid) and we use sophisticated methods to account for this and to improve

405 estimates. However, with an accurate geoid model the derivation of the mean is more robust  
406 and not so sensitive to i.e., use of various tracks in the lake and editing of point along the track.  
407 This makes the estimation of hydrological parameters like the time variation of the lake level  
408 more robust. Furthermore, for hydrodynamic modelling, each individual observation is  
409 important to model simulation. Geoid errors of decimeter could affect surface slope, which in  
410 turn will result in different water levels.

411 Thanks to the geodetic CryoSat-2 and SARAL missions, we are able to retrieve a local  
412 geoid correction, which can be used to improve the resolution of gravity field solutions at  
413 regions where terrestrial data are absent (i.e. “fill-in” values of EGM2008), and thus improve  
414 altimetry derived WSE for hydrological and hydrodynamic purposes. As concluded by Kingdon  
415 et al. (2008) altimetry does provide a higher resolution gravity field than satellite-derived (e.g.  
416 GRACE and GOCE) gravity fields and it will be a useful tool to determine a spatially finer  
417 equipotential field of large inland lakes. In addition, the forthcoming Surface Water and Ocean  
418 Topography (SWOT) mission with wide-swath can make it possible to derive more accurate  
419 local geoid undulation.

## 420 **5. Summary and conclusions**

421 The aim of this study was to **to** retrieve local geoid correction of inland waters over rugged  
422 topography. The enhanced geoid leads to a more accurate WSE over lakes, which could be  
423 beneficial for hydrologic and hydrodynamic applications.

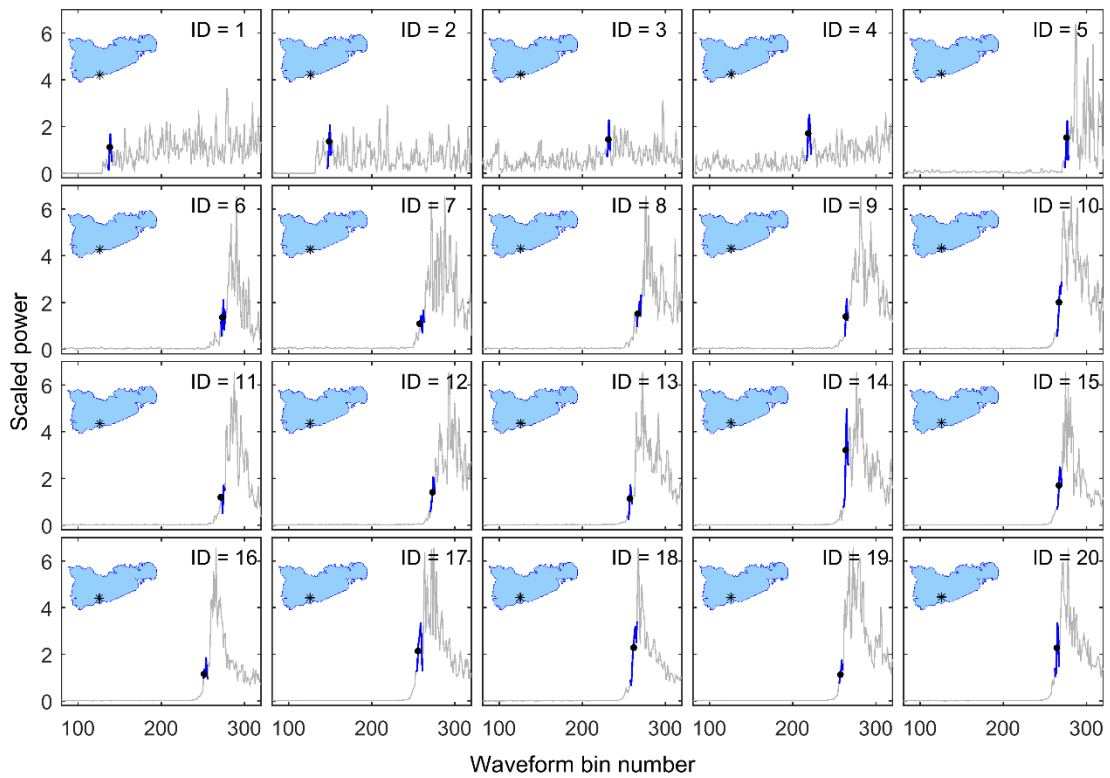
424 We used altimetry data from four missions, i.e. CryoSat-2, SARAL, Sentinel-3, and  
425 ICESat to derive water levels over Namco. We found that CryoSat-2 overestimates WSE  
426 nearshore and SARAL misses measurements close to the lakeshore. CryoSat-2 in SARIn mode  
427 does not perform as well as SARAL even though the former has a smaller along-track footprint.  
428 The measurements do not represent the lake level even at 5 km from the lakeshore probably  
429 due to the CryoSat-2 processor, onboard tracking system, or combination of both. In contrast,  
430 Sentinel-3 is not affected when the measurements are acquired at coast regions.

431 We compared the influence of the geoid on altimetry-derived WSE. To investigate the  
432 local geoid residual on WSE precision, we retrieved a local geoid signal from CryoSat-2 and  
433 SARAL-DF height anomaly. We found that geodetic altimetry data indeed contain geoid  
434 information and can be used to improve global geoid models over large lakes. Using high  
435 resolution altimetry data sets, i.e., ICESat, SARAL, and Sentinel-3, we validated our improved  
436 geoid model. The local geoid correction filed effectively reduced the uncertainty of ICESat,  
437 SARAL, and Sentinel-3 retrievals by 9%, 37%, and 14%, respectively. In addition, the accuracy  
438 of CryoSat-2 is improved by 8% and achieves a good agreement with in-situ data in terms of  
439 RMSE around 10 cm.

#### 440 **Acknowledgements**

441 The authors wish to acknowledge ESA, CNES/AVISO, and University of Bristol for providing  
442 CryoSat-2, SARAL, Sentinel-3, and ICESat datasets. Special thanks go to the ESA GPOD team  
443 who provided us L1b stack data set through the SARvatore platform. The first author is funded  
444 by China Scholarship Council, which is greatly acknowledged. The authors would like to thank  
445 Marcel Kleinherenbrink and two anonymous reviewers for their constructive comments and  
446 suggestions that helped to improve the quality of the manuscript.

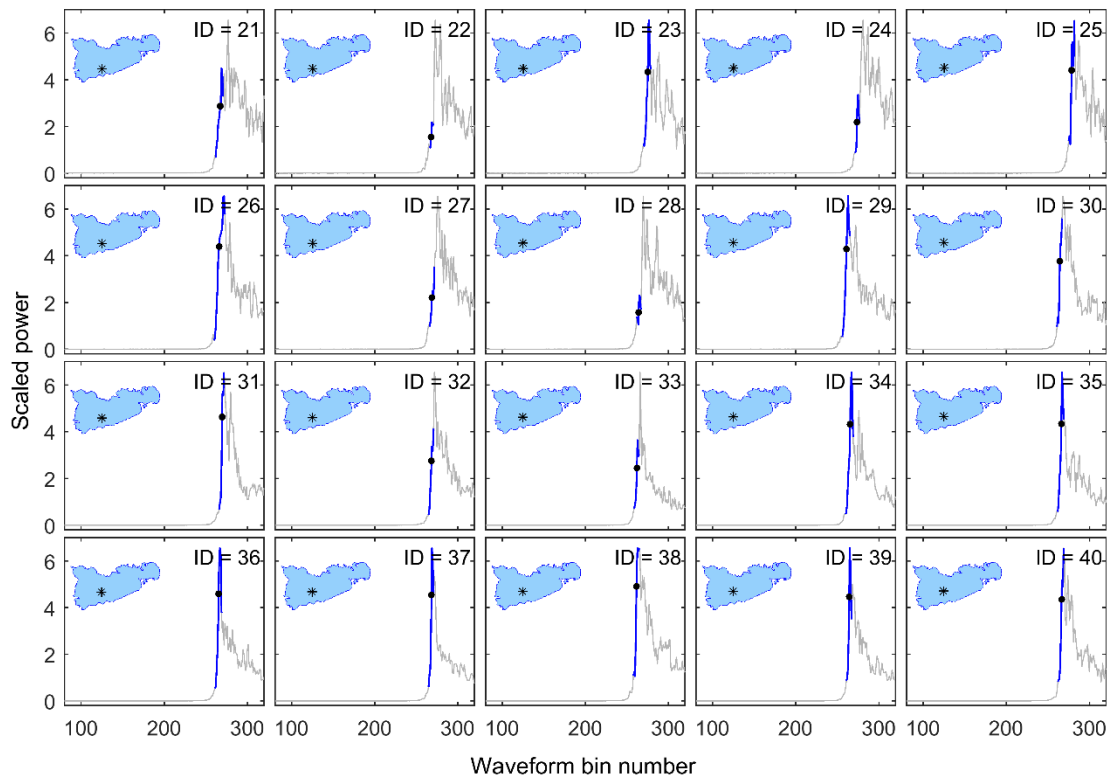
447 **Appendix A.** Illustration of waveforms of CryoSat-2. Below we show waveform performance  
448 of the first 20 measurements, middle open water, and the last 20 measurements close to  
449 lakeshore. In the following figures, we only show part of the waveforms to demonstrate the  
450 leading edge and retracking position.



451

452 **Fig. A1.** Waveforms of the first 20 measurements. Corresponding to ascending group 3 shown  
 453 in Fig. 1. Location of individual waveform is also shown in inset. Grey line indicates the  
 454 waveform, and blue line shows the retracked leading edge. Black dot indicates the retracked  
 455 bin. The first 5 messy waveforms are probably due to that the tracking window is not correctly  
 456 positioned.

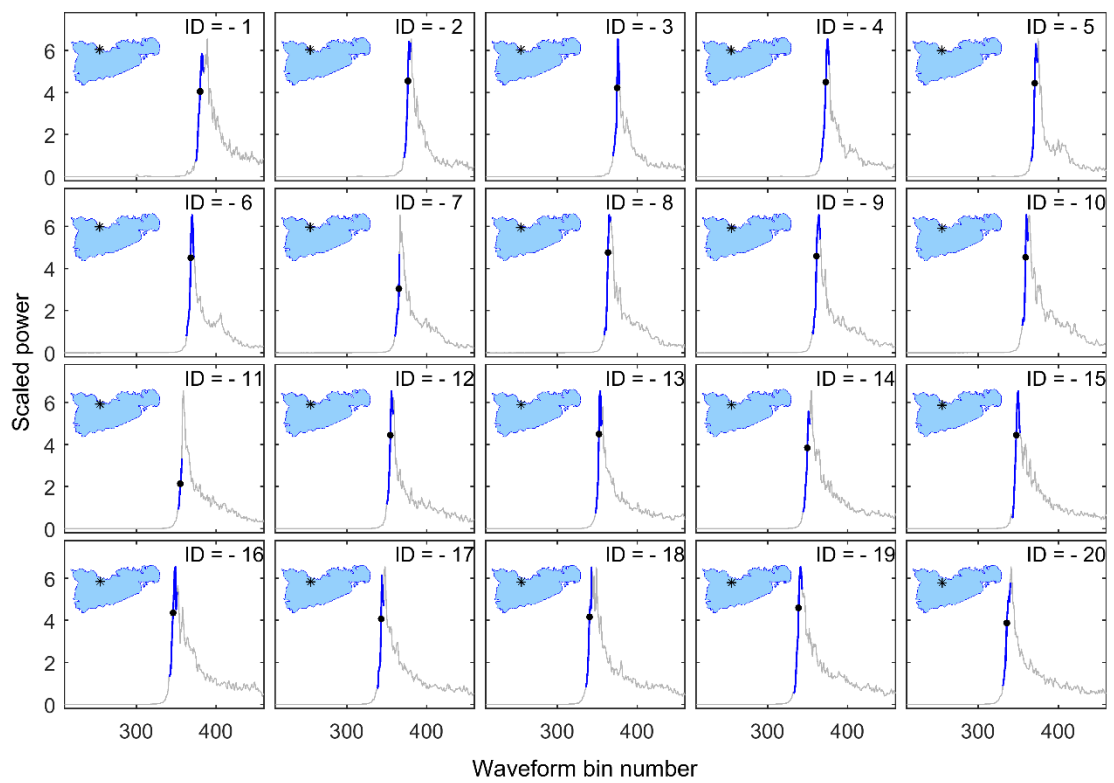
457



458

459 **Fig. A2.** Similar to Fig. A1, but for open water.

460

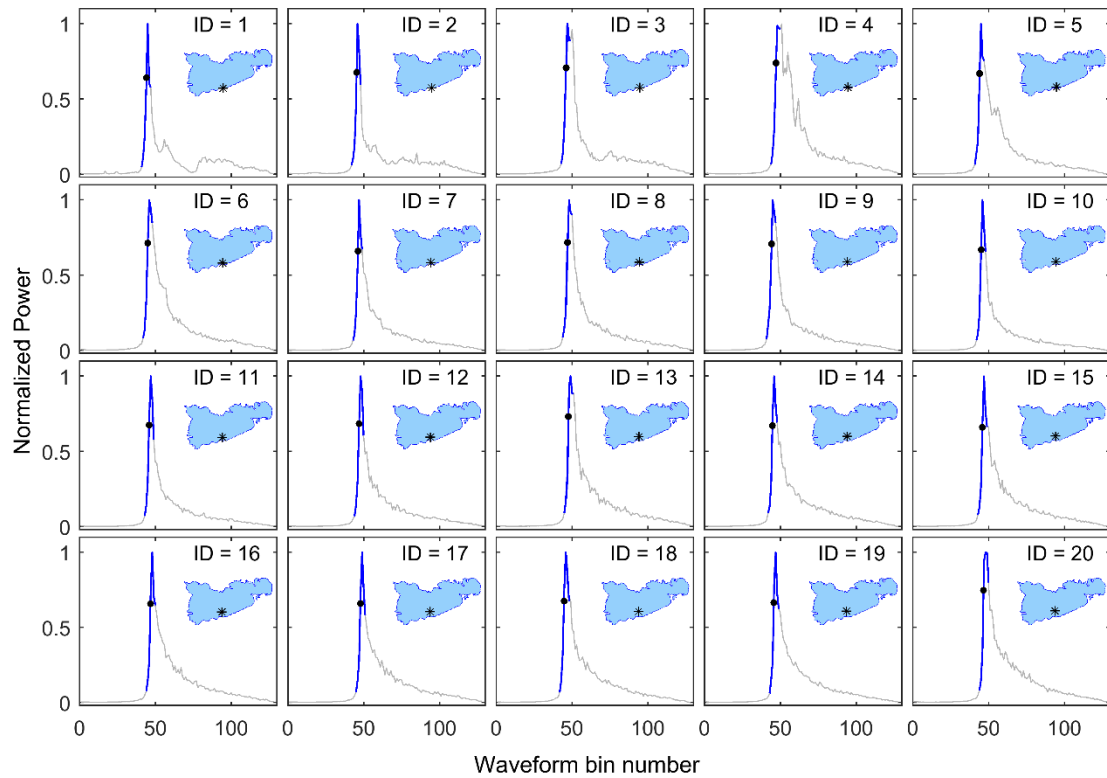


461

462 **Fig. A3.** Similar to Fig. A1, but for last 20 waveforms, indicated by negative numbers. The  
463 waveforms are very good even though they are acquired very close to lakeshore.

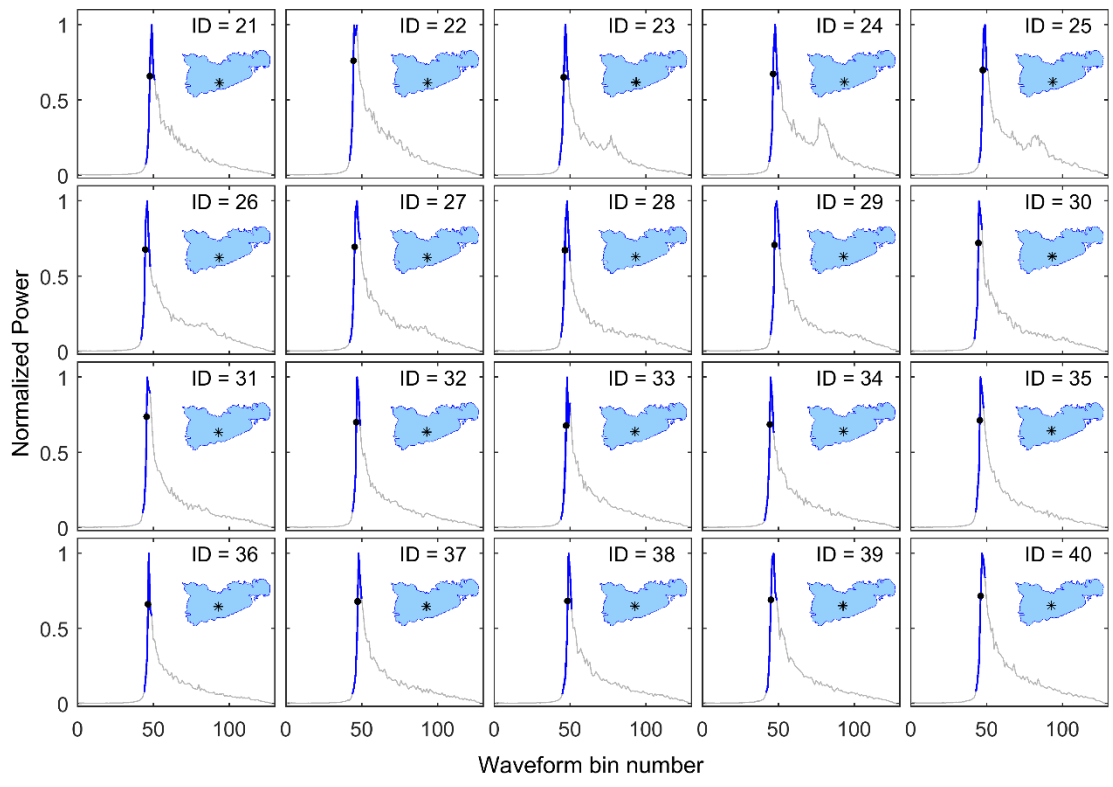
464

465 **Appendix B.** Illustration of waveforms of Sentinel-3 as a counterpart to CryoSat-2.



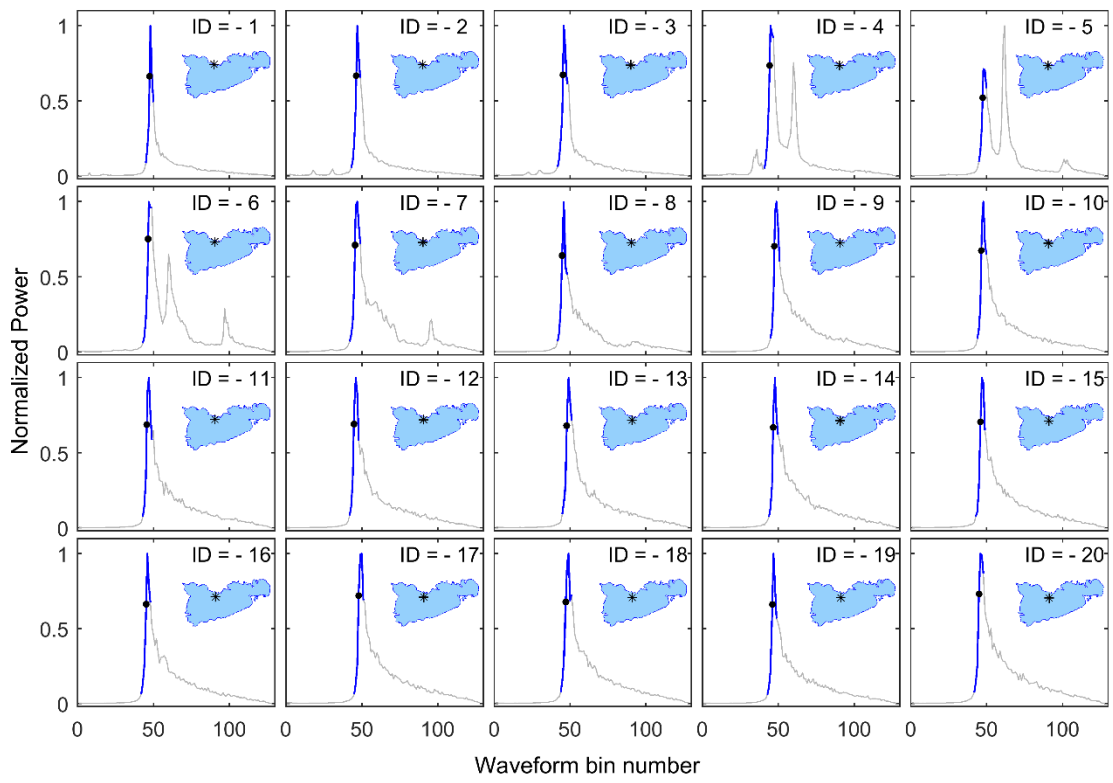
466

467 **Fig. B1.** Waveforms of the first 20 measurements. Corresponding to tracks shown in Fig. 9.  
468 Location of individual waveform is also shown in inset. Grey line indicates the whole  
469 waveform, and blue line shows the retracted leading edge. Black dot indicates the retracted  
470 bin.



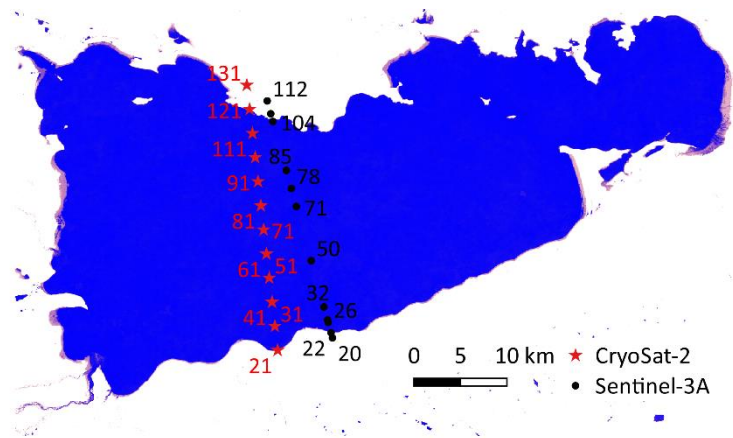
471

472 **Fig. B2.** Similar to B1, but for open water.



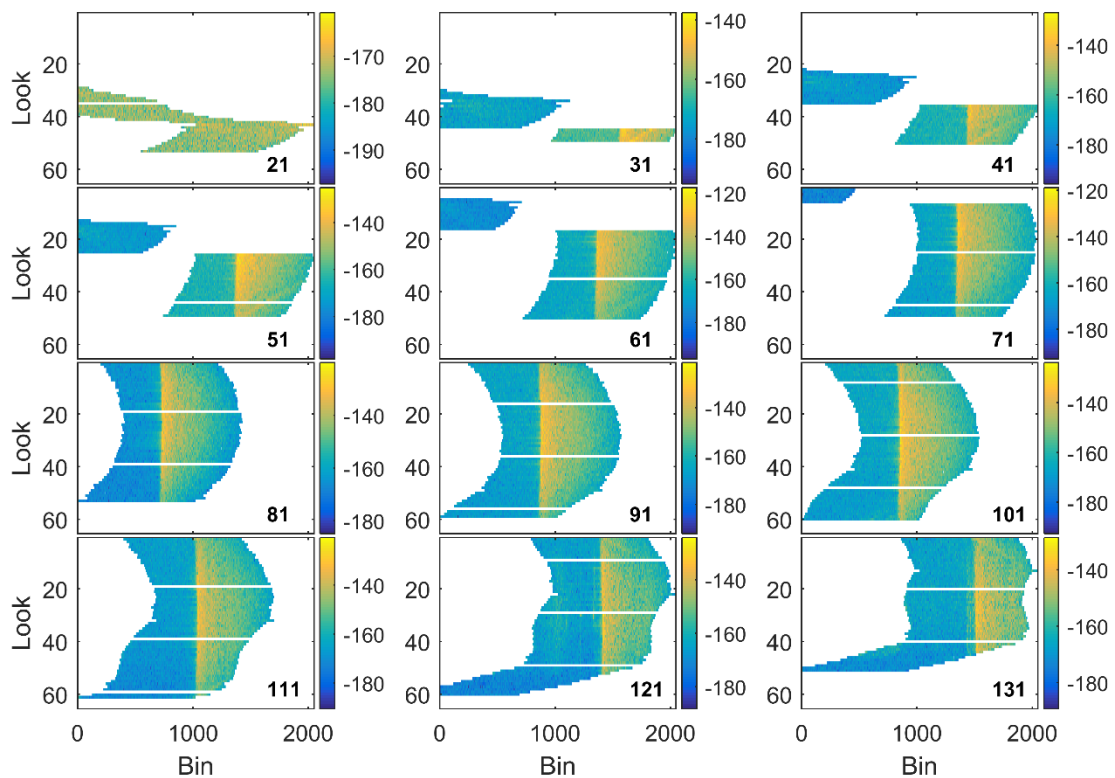
473

474 **Fig. B3.** Similar to B1, but for the last 20 waveforms.



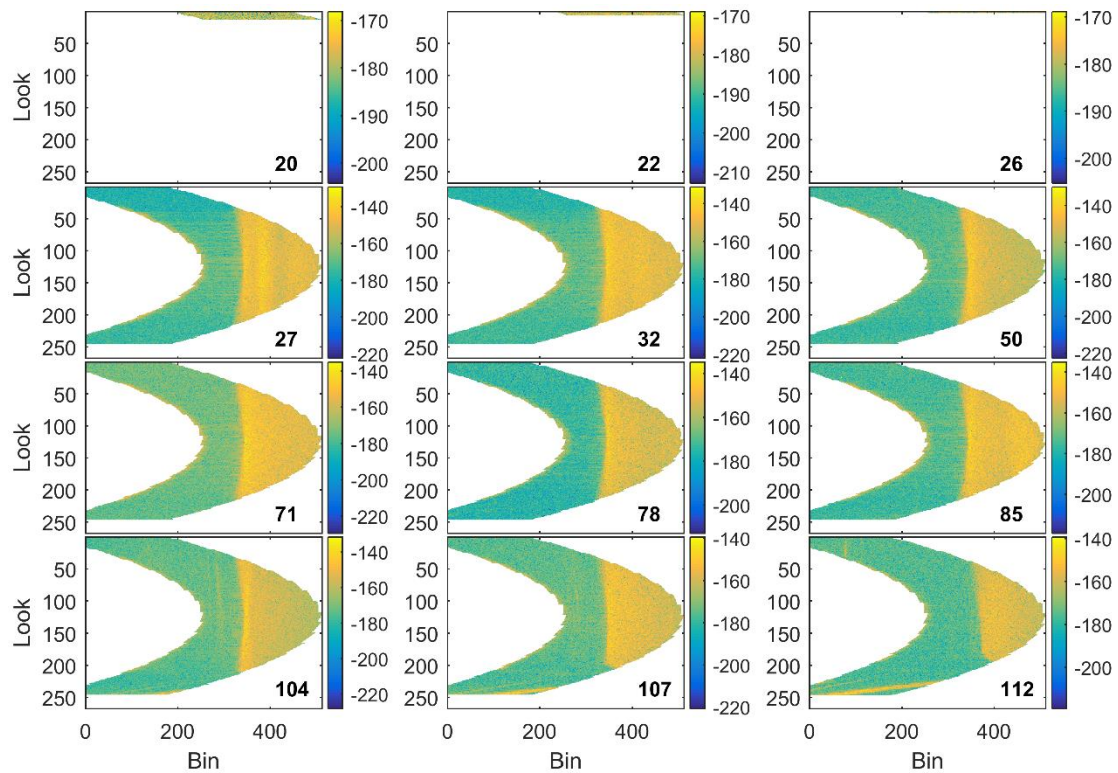
476

477 **Fig. C1.** Locations of measurements from CryoSat-2 and Sentinel-3A



478

479 **Fig. C2.** Some examples of CryoSat-2 SARIn stack data demonstrating the issue of noisy data  
 480 along the coast, color scale in dB and number referring to Fig. C1. The echoes from the point  
 481 targets remain with the antenna beam width for about 2 s, i.e. approximately 15 km in  
 482 orbit. The first look is from the extreme forward-looking Doppler beams and the last one from  
 483 the extreme backward-looking beams.



484

485 **Fig. C3.** Illustration of Sentinel-3 SAR stack of Doppler beams (looks) as colored images,  
 486 color scale in dB. Some looks are discarded out by means of a noise thresholding or of  
 487 Doppler angle thresholding. Number in each sub plot refers to Fig. C1.

488 **References**

489 Abulaitijiang, A., Andersen, O.B., Stenseng, L., 2015. Coastal sea level from inland CryoSat-  
 490 2 interferometric SAR altimetry. *Geophys. Res. Lett.* 42, 1841–1847.  
 491 doi:10.1002/2015GL063131

492 Akyilmaz, O., Özlüdemir, M.T., Ayan, T., Çelik, R.N., 2009. Soft computing methods for  
 493 geoidal height transformation. *Earth, Planets Sp.* 61, 825–833. doi:10.1186/BF03353193

494 Alsdorf, D.E., Rodriguez, E., Lettenmaier, D.P., 2007. Measuring surface water from space.  
 495 *Rev. Geophys.* 45, 1–24. doi:10.1029/2006RG000197.1.INTRODUCTION

496 Biancamaria, S., Frappart, F., Leleu, A.-S., Marieu, V., Blumstein, D., Desjonquères, J.-D.,  
497 Boy, F., Sottolichio, A., Valle-Levinson, A., 2017. Satellite radar altimetry water  
498 elevations performance over a 200m wide river: Evaluation over the Garonne River.  
499 Adv. Sp. Res. 59, 128–146. doi:10.1016/j.asr.2016.10.008

500 Blewitt, G., Kreemer, C., Hammond, W.C., Gazeaux, J., 2016. MIDAS robust trend estimator  
501 for accurate GPS station velocities without step detection. J. Geophys. Res. Solid Earth  
502 121, 2054–2068. doi:10.1002/2015JB012552

503 Bonnefond, P., Verron, J., Aublanc, J., Babu, K., Bergé-Nguyen, M., Cancet, M., Chaudhary,  
504 A., Crétaux, J.-F., Frappart, F., Haines, B., Laurain, O., Ollivier, A., Poisson, J.-C.,  
505 Prandi, P., Sharma, R., Thibaut, P., Watson, C., 2018. The Benefits of the Ka-Band as  
506 Evidenced from the SARAL/AltiKa Altimetric Mission: Quality Assessment and  
507 Unique Characteristics of AltiKa Data. Remote Sens. 10, 83. doi:10.3390/rs10010083

508 Brenner, A.C., DiMarzio, J.P., Zwally, H.J., 2007. Precision and accuracy of satellite radar  
509 and laser altimeter data over the continental ice sheets. IEEE Trans. Geosci. Remote  
510 Sens. 45, 321–331. doi:10.1109/TGRS.2006.887172

511 Chelton, D.B., Ries, J.C., Haines, B.J., Fu, L.-L., Callahan, P.S., 2001. Satellite Altimetry, in:  
512 Satellite Altimetry and Earth Sciences: A Handbook of Techniques and Applications.  
513 pp. 2504–2510. doi:10.1016/S0074-6142(01)80146-7

514 CNES, 2016. SARAL / AltiKa Products Handbook.

515 Crétaux, J.F., Jelinski, W., Calmant, S., Kouraev, A., Vuglinski, V., Bergé-Nguyen, M.,

516 Gennero, M.C., Nino, F., Abarca Del Rio, R., Cazenave, A., Maisongrande, P., 2011.  
517 SOLS: A lake database to monitor in the Near Real Time water level and storage  
518 variations from remote sensing data. *Adv. Sp. Res.* 47, 1497–1507.  
519 doi:10.1016/j.asr.2011.01.004

520 Dehecq, A., Gourmelen, N., Shepherd, A., Cullen, R., Trouvé, E., 2013. Evaluation of  
521 CryoSat-2 for height retrieval over the Himalayan range, in: *CryoSat-2 Third User*  
522 *Workshop*, March 2013. Dresden, Germany.

523 Dinardo, S., Benveniste, J., 2013. Guidelines for the SAR (Delay-Doppler) L1b Processing.

524 Dingman, S., 2015. *Physical hydrology*, Third Edit. ed.

525 Erol, B., 2011. An automated height transformation using precise geoid models. *Sci. Res.*  
526 *Essays* 6, 1351–1363. doi:10.5897/SRE10.1119

527 European Space Agency, Mullar Space Science Laboratory, 2012. *CryoSat Product*  
528 *Handbook*.

529 Fecher, T., Pail, R., Gruber, T., Schuh, W.D., Kusche, J., Brockmann, J.M., Loth, I., Müller,  
530 S., Eicker, A., Schall, J., Mayer-Gürr, T., Kvas, A., Klinger, B., Rieser, D., Zehentner,  
531 N., Baur, O., Höck, E., Krauss, S., Jäggi, A., Meyer, U., Prange, L., Maier, A., 2017.  
532 GOCO05c: A New Combined Gravity Field Model Based on Full Normal Equations  
533 and Regionally Varying Weighting. *Surv. Geophys.* 38, 571–590. doi:10.1007/s10712-  
534 016-9406-y

535 Forsberg, R., 1985. Gravity field terrain effect computations by FFT. *Bull. Géodésique* 59,

536 342–360. doi:10.1007/BF02521068

537 Heiskanen, W.A., Moritz, H., 1967. Physical geodesy. W. H. Freeman & Co Ltd, San  
538 Francisco and London.

539 Hirt, C., 2011. Assessment of EGM2008 over Germany using accurate quasigeoid heights  
540 from vertical deflections, GCG05 and GPS/levelling. ZFV - Zeitschrift für Geodäsie,  
541 Geoinf. und Landmanagement 136, 138–149.

542 Hirt, C., Featherstone, W.E., Marti, U., 2010. Combining EGM2008 and SRTM/DTM2006.0  
543 residual terrain model data to improve quasigeoid computations in mountainous areas  
544 devoid of gravity data. J. Geod. 84, 557–567. doi:10.1007/s00190-010-0395-1

545 Hwang, C., Cheng, Y.-S., Han, J., Kao, R., Huang, C.-Y., Wei, S.-H., Wang, H., 2016. Multi-  
546 Decadal Monitoring of Lake Level Changes in the Qinghai-Tibet Plateau by the  
547 TOPEX/Poseidon-Family Altimeters: Climate Implication. Remote Sens. 8, 446.  
548 doi:10.3390/rs8060446

549 Jain, M., Andersen, O.B., Dall, J., Stenseng, L., 2015. Sea surface height determination in the  
550 Arctic using Cryosat-2 SAR data from primary peak empirical retracker. Adv. Sp. Res.  
551 55, 40–50. doi:10.1016/j.asr.2014.09.006

552 Jiang, L., Nielsen, K., Andersen, O.B., Bauer-Gottwein, P., 2017a. Monitoring recent lake  
553 level variations on the Tibetan Plateau using CryoSat-2 SARIn mode data. J. Hydrol.  
554 544, 109–124. doi:10.1016/j.jhydrol.2016.11.024

555 Jiang, L., Nielsen, K., Andersen, O.B., Bauer-Gottwein, P., 2017b. CryoSat-2 radar altimetry

556 for monitoring China's freshwater resources. *Remote Sens. Environ.* 200, 125–139.  
557 doi:10.1016/j.rse.2017.08.015

558 Jiang, L., Schneider, R., Andersen, O.B., Bauer-Gottwein, P., 2017c. CryoSat-2 Altimetry  
559 Applications over Rivers and Lakes. *Water* 9, 211. doi:10.3390/w9030211

560 Ke, C.-Q., Tao, A.-Q., Jin, X., 2013. Variability in the ice phenology of Nam Co Lake in  
561 central Tibet from scanning multichannel microwave radiometer and special sensor  
562 microwave/imager: 1978 to 2013. *J. Appl. Remote Sens.* 7, 073477.  
563 doi:10.1117/1.JRS.7.073477

564 Kingdon, R., Hwang, C., Hsiao, Y.S., Santos, M., 2008. Gravity anomalies from retracked  
565 ERS and geosat altimetry over the Great Lakes: Accuracy assessment and problems.  
566 *Terr. Atmos. Ocean. Sci.* 19, 93–101. doi:10.3319/TAO.2008.19.1-2.93(SA)

567 Kleinherenbrink, M., Ditmar, P.G., Lindenbergh, R.C., 2014. Retracking Cryosat data in the  
568 SARIn mode and robust lake level extraction. *Remote Sens. Environ.* 152, 38–50.  
569 doi:10.1016/j.rse.2014.05.014

570 Kropáček, J., Maussion, F., Chen, F., Hoerz, S., Hochschild, V., 2013. Analysis of ice  
571 phenology of lakes on the Tibetan Plateau from MODIS data. *Cryosph.* 7, 287–301.  
572 doi:10.5194/tc-7-287-2013

573 Lei, Y., Yao, T., Bird, B.W., Yang, K., Zhai, J., Sheng, Y., 2013. Coherent lake growth on the  
574 central Tibetan Plateau since the 1970s: Characterization and attribution. *J. Hydrol.* 483,  
575 61–67. doi:10.1016/j.jhydrol.2013.01.003

576 Leys, C., Ley, C., Klein, O., Bernard, P., Licata, L., 2013. Detecting outliers: Do not use  
577 standard deviation around the mean, use absolute deviation around the median. *J. Exp.*  
578 *Soc. Psychol.* 49, 764–766. doi:10.1016/j.jesp.2013.03.013

579 Li, J., Shen, W., Zhou, X., 2015. Direct regional quasi-geoid determination using EGM2008  
580 and DEM: A case study for Mainland China and its vicinity areas. *Geod. Geodyn.* 6,  
581 437–443. doi:10.1016/j.geog.2015.12.002

582 Mazloff, M.R., Gille, S.T., Cornuelle, B., 2014. Improving the geoid: Combining altimetry  
583 and mean dynamic topography in the California coastal ocean. *Geophys. Res. Lett.* 41,  
584 8944–8952. doi:10.1002/2014GL062402

585 Meyer, T.H., Roman, D.R., Zilkoski, D.B., Meyer, T.H., Roman, D.R., David, B., 2006. What  
586 Does Height Really Mean? Part III: Height Systems. *Surv. L. Inf. Sci.* 66, 149–160.

587 National Geodetic Survey, 1986. *Geodetic glossary*. U.S. Dept. of Commerce, National  
588 Oceanic and Atmospheric Administration, National Ocean Service, Charting and  
589 Geodetic Services, 1986.

590 Nielsen, K., Stenseng, L., Andersen, O.B., Knudsen, P., 2017. The Performance and  
591 Potentials of the CryoSat-2 SAR and SARIn Modes for Lake Level Estimation. *Water* 9,  
592 374. doi:10.3390/w9060374

593 Nielsen, K., Stenseng, L., Andersen, O.B., Villadsen, H., Knudsen, P., 2015. Validation of  
594 CryoSat-2 SAR mode based lake levels. *Remote Sens. Environ.* 171, 162–170.  
595 doi:10.1016/j.rse.2015.10.023

596 Pavlis, N.K., Holmes, S.A., Kenyon, S.C., Factor, J.K., 2012. The development and  
597 evaluation of the Earth Gravitational Model 2008 (EGM2008). *J. Geophys. Res. Solid*  
598 *Earth* 117, n/a-n/a. doi:10.1029/2011JB008916

599 Schneider, R., Godiksen, P.N., Villadsen, H., Madsen, H., Bauer-Gottwein, P., 2017.  
600 Application of CryoSat-2 altimetry data for river analysis and modelling. *Hydrol. Earth*  
601 *Syst. Sci.* 21, 751–764. doi:10.5194/hess-21-751-2017

602 Schneider, R., Ridler, M.E., Godiksen, P.N., Madsen, H., Bauer-Gottwein, P., 2018a. A data  
603 assimilation system combining CryoSat-2 data and hydrodynamic river models. *J.*  
604 *Hydrol.* 557, 197–210. doi:10.1016/j.jhydrol.2017.11.052

605 Schneider, R., Tarpanelli, A., Nielsen, K., Madsen, H., Bauer-Gottwein, P., 2018b. Evaluation  
606 of multi-mode CryoSat-2 altimetry data over the Po River against in situ data and a  
607 hydrodynamic model. *Adv. Water Resour.* 112, 17–26.  
608 doi:10.1016/j.advwatres.2017.11.027

609 Schwatke, C., Dettmering, D., Bosch, W., Seitz, F., 2015. DAHITI - An innovative approach  
610 for estimating water level time series over inland waters using multi-mission satellite  
611 altimetry. *Hydrol. Earth Syst. Sci.* 19, 4345–4364. doi:10.5194/hess-19-4345-2015

612 Seo, D., Sigdel, R., Kwon, K.H., Lee, Y.S., 2010. 3-D hydrodynamic modeling of Yongdam  
613 Lake, Korea using EFDC. *Desalin. Water Treat.* 19, 42–48. doi:10.5004/dwt.2010.1894

614 She, Y., Fu, G., Wang, Z., Liu, T., Xu, C., Jin, H., 2016. Gravity anomalies and lithospheric  
615 flexure around the Longmen Shan deduced from combinations of in situ observations

616 and EGM2008 data. *Earth, Planets Sp.* 68, 163. doi:10.1186/s40623-016-0537-7

617 Song, C., Huang, B., Ke, L., Richards, K.S., 2014. Seasonal and abrupt changes in the water  
618 level of closed lakes on the Tibetan Plateau and implications for climate impacts. *J.*  
619 *Hydrol.* 514, 131–144. doi:10.1016/j.jhydrol.2014.04.018

620 Steunou, N., Desjonqueres, J.D., Picot, N., Sengenes, P., Noubel, J., Poisson, J.C., 2015.  
621 *AltiKa Altimeter: Instrument Description and In Flight Performance. Mar. Geod.* 38,  
622 22–42. doi:10.1080/01490419.2014.988835

623 Tseng, K.H., Chang, C.P., Shum, C.K., Kuo, C.Y., Liu, K.T., Shang, K., Jia, Y., Sun, J.,  
624 2016. Quantifying freshwater mass balance in the central Tibetan Plateau by integrating  
625 satellite remote sensing, altimetry, and gravimetry. *Remote Sens.* 8.  
626 doi:10.3390/rs8060441

627 Villadsen, H., Deng, X., Andersen, O.B., Stenseng, L., Nielsen, K., Knudsen, P., 2016.  
628 Improved inland water levels from SAR altimetry using novel empirical and physical  
629 retrackers. *J. Hydrol.* 537, 234–247. doi:10.1016/j.jhydrol.2016.03.051

630 Wang, J., Zhu, L., Daut, G., Ju, J., Lin, X., Wang, Y., Zhen, X., 2009. Investigation of  
631 bathymetry and water quality of Lake Nam Co, the largest lake on the central Tibetan  
632 Plateau, China. *Limnology* 10, 149–158. doi:10.1007/s10201-009-0266-8

633 Wingham, D.J., Francis, C.R., Baker, S., Bouzinac, C., Brockley, D., Cullen, R., de Chateau-  
634 Thierry, P., Laxon, S.W., Mallow, U., Mavrocordatos, C., Phalippou, L., Ratier, G.,  
635 Rey, L., Rostan, F., Viau, P., Wallis, D.W., 2006. CryoSat: A mission to determine the

636 fluctuations in Earth's land and marine ice fields. *Adv. Sp. Res.* 37, 841–871.  
637 doi:10.1016/j.asr.2005.07.027

638 Xue, P., Pal, J.S., Ye, X., Lenters, J.D., Huang, C., Chu, P.Y., 2017. Improving the  
639 Simulation of Large Lakes in Regional Climate Modeling: Two-Way Lake–Atmosphere  
640 Coupling with a 3D Hydrodynamic Model of the Great Lakes. *J. Clim.* 30, 1605–1627.  
641 doi:10.1175/JCLI-D-16-0225.1

642 Yilmaz, N., 2008. Comparison of different height systems. *Geo-spatial Inf. Sci.* 11, 209–214.  
643 doi:10.1007/s11806-008-0074-z

644 Zandagba, J., Moussa, M., Obada, E., Afouda, A., 2016. Hydrodynamic Modeling of Nokoué  
645 Lake in Benin. *Hydrology* 3, 44. doi:10.3390/hydrology3040044

646 Zhang, G., Xie, H., Kang, S., Yi, D., Ackley, S.F., 2011. Monitoring lake level changes on the  
647 Tibetan Plateau using ICESat altimetry data (2003-2009). *Remote Sens. Environ.* 115,  
648 1733–1742. doi:10.1016/j.rse.2011.03.005

649 Zlinszky, A., Timár, G., Weber, R., Székely, B., Briese, C., Ressler, C., Pfeifer, N., 2014.  
650 Observation of a local gravity potential isosurface by airborne lidar of lake Balaton,  
651 Hungary. *Solid Earth* 5, 355–369. doi:10.5194/se-5-355-2014

652 Zwally, H.J., Schutz, B., Abdalati, W., Abshire, J., Bentley, C., Brenner, A., Bufton, J.,  
653 Dezio, J., Hancock, D., Harding, D., Herring, T., Minster, B., Quinn, K., Palm, S.,  
654 Spinhrne, J., Thomas, R., 2002. ICESat's laser measurements of polar ice, atmosphere,  
655 ocean, and land. *J. Geodyn.* 34, 405–445. doi:10.1016/S0264-3707(02)00042-X

656 Zwally, H.J., Yi, D., Kwok, R., Zhao, Y., 2008. ICESat measurements of sea ice freeboard

657 and estimates of sea ice thickness in the Weddell Sea. *J. Geophys. Res.* 113, C02S15.

658 doi:10.1029/2007JC004284

659